

QUANTITATIVE ESTIMATES OF MINIMUM CORE MASSES FOR GIANT PLANET FORMATION

ANA-MARIA A. PISO
 Harvard-Smithsonian Center for Astrophysics

ANDREW N. YODIN
 JILA, University of Colorado at Boulder

RUTH A. MURRAY-CLAY
 Harvard-Smithsonian Center for Astrophysics
Draft version October 23, 2013

ABSTRACT

The core accretion model postulates that giant planets form through accretion of gas onto a solid core. When a core embedded in a protoplanetary disk accretes an atmosphere with mass comparable to itself, the envelope is no longer in hydrostatic balance and unstable atmosphere collapse occurs. Formation of a core requires rapid planetesimal accretion, which deposits energy into the atmosphere. Heating increases the core mass required for collapse. However, the planetesimal accretion rate need not be constant — in particular, it may decline over time. In this study we consider the limiting regime in which planetesimal accretion is negligible and the luminosity evolution of a core’s atmosphere is dominated by Kelvin-Helmholtz contraction. We enhance the model of Piso & Youdin (submitted), which derives the evolution of atmospheres embedded in a gas disk, to employ a more realistic equation of state and dust opacity. We find that the minimum core mass required to form a giant planet before the dissipation of the protoplanetary disk increases by more than a factor of two when non-ideal effects such as hydrogen dissociation and quantum rotational effects are included in the equation of state, when compared to an ideal gas polytrope. However, this minimum core mass decreases back to $M_{\text{c,crit}} \sim 5M_{\oplus}$ once we assume realistic dust opacities that take into account grain growth. Our results yield lower critical core masses than corresponding studies for large planetesimal accretion rates. We therefore conclude that it is easier to form a planet by growing the core first, then accreting a massive gaseous envelope, rather than forming the core and atmosphere simultaneously.

1. INTRODUCTION

One of the prevalent theories of giant planet formation is the core accretion model (e.g., Mizuno et al. 1978, Stevenson 1982, Bodenheimer & Pollack 1986, D’Angelo et al. 2011). It stipulates that Jupiter-sized planets form due to accretion of planetesimals into a solid core that grows large enough to attract a massive atmosphere.

In models that assume a high planetesimal accretion rate (e.g., Rafikov 2006), the gaseous envelope is heated solely by planetesimals and is therefore in a steady state at all times, in which all the incoming energy due to planetesimals is radiated away. In this regime, the core and atmosphere grow simultaneously, with the atmosphere increasing in mass faster than the core. As the envelope and core become comparable in mass, hydrostatic balance no longer holds and a rapid phase of unstable atmosphere collapse commences. The maximum core mass for which the atmosphere is still in hydrostatic equilibrium is defined in these studies as the “critical core mass”. For a fixed planetesimal accretion rate and a set of disk conditions, the critical core mass is uniquely determined.

Time-dependent core accretion models (e.g., Pollack et al. 1996, Ikoma et al. 2000) include variable planetesimal rates which allow for the Kelvin-Helmholtz (KH) contraction of the gaseous envelope to become important. In this regime, the atmosphere luminosity is not only supplied by planetesimals, but also by gas contrac-

tion. The envelope is no longer in a steady state, but rather it accretes gas as it cools. Pollack et al. (1996) find that the evolution of a giant planet can be separated into three phases. The core forms during phase 1 due to runaway planetesimal accretion, while the envelope mass stays small. Once the planet’s feeding zone has been depleted of solids, planetesimal accretion is significantly reduced and can no longer balance radiative losses. As a result, the atmosphere cools while undergoing KH contraction; this is phase 2. The envelope mass now steadily increases while core growth is stalled. Runaway gas accretion begins once the atmosphere mass is comparable to the core mass in phase 3. Pollack et al. (1996) find that phase 2 lasts much longer than phases 1 and 3, and so the evolutionary timescale of the planet is set by KH contraction. Studying atmosphere growth onto a solid core of fixed mass (e.g., Papaloizou & Nelson 2005) can thus provide accurate estimates for the timescale required to form a giant planet.

Piso & Youdin (submitted; hereafter Paper I) study atmosphere evolution around a fully grown core with fixed mass, assuming the luminosity of the envelope is solely due to KH contraction while planetesimal accretion is neglected. They build quasi-static two-layer atmosphere models, and derive a cooling model to connect static profiles in time and obtain an evolutionary history. They define the time t at which unstable atmosphere collapse commences as the *crossover time* t_{co} , at

which $M_{\text{atm}}(t_{\text{co}}) \sim M_c$. From this they define as *critical core mass* the minimum core mass for a protoplanet to undergo runaway gas accretion during the lifetime of the disk. They calculate the critical core mass for a variety of disk conditions, nebular gas compositions and opacities, and find that the critical core mass is smaller for lower disk temperatures (i.e., larger stellocentric distances), lower opacities and larger mean molecular weight of the gas.

This study builds on the results of Paper I by making two important additions: we include realistic equation of state (EOS) effects, as well as realistic dust opacities.

Paper I assumes that the nebular gas is an ideal diatomic gas described by a polytropic equation of state (EOS). However, non-ideal effects such as dissociation and ionization have to be taken into account in order to obtain better quantitative results. In this study, we consider atmosphere growth assuming that the nebular gas is described by a realistic EOS given by the Saumon et al. (1995) EOS tables, and determine the critical core mass for a giant planet to form before the dissipation of the protoplanetary disk. We find that the critical core mass is more than twice as large than in the ideal case if realistic thermodynamic effects are taken into account.

Another simplification in Paper I is the assumption that the dust opacity in radiative regions is that of interstellar grains. In reality, opacities in protoplanetary disks, while not tightly constrained observationally, are unlikely to be interstellar. As we consider a regime of low planetesimal accretion in which solids have been segregated from the gas and are not being added back in, it is likely that the grain opacity will be lower than the standard interstellar medium (ISM) opacity. This effect is explored in Paper I, and it is found that a factor of ten opacity reduction results in a critical core mass twice as small. In this study, we use realistic opacity tables that are calculated based on observations of protoplanetary disks and take into account grain growth. We find that the resulting critical core mass may be significantly lower when ISM opacities are used, i.e. by more than a factor of three at 5 AU, and around 1.5 times lower at 100 AU.

This paper is organized as follows. In section §2 we review the quasi-static and cooling models derived in Paper I. We discuss the variations in the adiabatic gradient caused by non-ideal EOS effects in section §3, and their implications for atmosphere evolution in section §4. We determine the minimum core mass to form a giant planet during the disk lifetime in section §5, with realistic EOS and dust opacity assumptions. In section §6 we compare our results to those obtained by studies that consider planetesimal accretion as the dominant source of energy. Finally, we summarize our findings in section §7.

2. MODEL REVIEW

In this section we review the model developed in Paper I for the structure and evolution of a planetary atmosphere embedded in a protoplanetary disk. We describe the assumptions of the model and the properties of our assumed protoplanetary disk in section §2.1, and we summarize the equations describing the structure and time evolution of the atmosphere in section §2.2.

2.1. Assumptions and Disk Model

We assume that the planet consists of a solid core of fixed mass and a two-layer atmosphere composed of an inner convective region and an outer radiative zone that matches smoothly onto the disk. The two regions are separated by the Schwarzschild criterion for convective instability (see section §2.2). We denote the surface between the two regions as the radiative-convective boundary (RCB), defined by a radius $r = R_{\text{RCB}}$. We assume a low planetesimal accretion regime in which the atmosphere evolution is dominated by KH contraction. Moreover, we assume that the luminosity is constant throughout the outer radiative region (see section §5 for additional discussion). The atmosphere is spherically symmetric, self-gravitating and in hydrostatic balance. We note that spherical symmetry confines us to the outer regions of the disk ($a \gtrsim 5$ AU), where the disk scale height is larger than the radius at which the planet matches onto the disk (see Paper I for further details). The nebular gas is composed of a hydrogen-helium mixture, with hydrogen and helium mass fractions of 0.7 and 0.3, respectively. We assume that the envelope evolves through stages of quasi-static equilibrium.

The temperature and pressure at the outer boundary of the atmosphere are given by the nebular temperature and pressure. As a disk model, we use the minimum mass, passively irradiated model of Chiang & Youdin (2010). The surface density, mid-plane temperature and mid-plane pressure are given by

$$\Sigma_d = 2200 (a/\text{AU})^{-3/2} \text{ g cm}^{-2} \quad (1a)$$

$$T_d = 120 (a/\text{AU})^{-3/7} \text{ K}, \quad (1b)$$

$$P_d = 110 (a/\text{AU})^{-45/14} \text{ dyn cm}^{-2} \quad (1c)$$

with a the semi-major axis and for a mean molecular weight $\mu = 2.35$.

2.2. Structure Equations and Cooling Model

The structure of a static atmosphere is described by the standard equations of hydrostatic balance and thermal equilibrium:

$$\frac{dP}{dr} = -\frac{Gm}{r^2} \rho \quad (2a)$$

$$\frac{dm}{dr} = 4\pi r^2 \rho \quad (2b)$$

$$\frac{dT}{dr} = \nabla \frac{T}{P} \frac{dP}{dr} \quad (2c)$$

$$\frac{dL}{dr} = 4\pi r^2 \rho (\epsilon + \epsilon_g), \quad (2d)$$

with r the radial coordinate, P , T and ρ the gas pressure, temperature and density, respectively, m the mass enclosed by the radius r , L the luminosity from the surface of radius r , and G the gravitational constant. The ϵ term represents the rate at which internal heat is generated per unit mass, while $\epsilon_g \equiv -T \frac{ds}{dt}$ is the heating per unit mass due to gravitational contraction, with s the specific gas entropy. We do not take into account any internal energy sources and set $\epsilon = 0$. The temperature gradient $\nabla \equiv \frac{d \ln T}{d \ln P}$ depends on whether energy is transported throughout the atmosphere by radiation

or convection. In the case of radiative diffusion for an optically thick gas, the temperature gradient is

$$\nabla = \nabla_{\text{rad}} \equiv \frac{3\kappa P}{64\pi G m \sigma T^4} L, \quad (3)$$

with σ the Stefan-Boltzmann constant and κ the dust opacity. In our models the atmosphere is optically thick throughout the outer boundary. Where energy is transported through convection the temperature gradient is given by

$$\nabla = \nabla_{\text{ad}} \equiv \left(\frac{d \ln T}{d \ln P} \right)_{\text{ad}}, \quad (4)$$

with ∇_{ad} the adiabatic temperature gradient. The convective and radiative layers of the envelope are separated by the Schwarzschild criterion (e.g., Thompson 2006): the atmosphere is stable against convection when $\nabla < \nabla_{\text{ad}}$ and convectively unstable when $\nabla > \nabla_{\text{ad}}$. For effective convection, $\nabla \approx \nabla_{\text{ad}}$. The temperature gradient is thus given by $\nabla = \min(\nabla_{\text{ad}}, \nabla_{\text{rad}})$.

The equation set (2) is supplemented by an equation of state (EOS) relating pressure, temperature and density, as well as an opacity law. Paper I assumes an ideal gas polytropic EOS, $P = K \rho^\gamma$, with K the adiabatic constant and γ the adiabatic index. In this study we use realistic EOS tables, as explained in section §3. Furthermore, Paper I assumes a power-law opacity given by

$$\kappa = 2F_\kappa \left(\frac{T}{T_{\text{ref}}} \right)^\beta, \quad (5)$$

with β and F_κ constants, and T_{ref} a normalizing temperature. To estimate β and F_κ we use the Bell & Lin (1994) opacity laws for ice grains: $\beta = 2$, $F_\kappa = 1$ and $T_{\text{ref}} = 100$ K. We note that these values are valid only for low disk temperatures, $T_d \lesssim 100$ K, where all dust components are present. Dust settling and grain growth lower both the normalization factor F_κ and the power-law coefficient β . In this paper, we explore more realistic opacity laws and their effect on the critical core mass when compared to the ISM power-law (5), as discussed in section §5.

We assume that the atmosphere forms around a solid core of fixed mass M_c with a radius $R_c = (3M_c/4\pi\rho_c)^{1/3}$, where ρ_c is the core density. We choose $\rho_c = 3.2$ g cm $^{-3}$ (e.g., Papaloizou & Terquem 1999). The atmosphere is assumed to match on to the protoplanetary disk at the

Hill radius $R_H \equiv a \left(\frac{M_p}{3M_\odot} \right)^{1/3}$, the distance at which the gravitational attraction of the planet and the tidal gravity due to the host star are equal. Outside the Hill sphere, the planet gravity is overcome by stellar tidal gravity, and hence only gas that lies within the Hill sphere can be gravitationally bound to the planet. The effective outer boundary of the atmosphere is the surface defined by the Bondi radius, $R_B \equiv \frac{GM_p}{c_s^2} = \frac{GM_p}{\mathcal{R}T_d}$. This is the distance from the planet at which the thermal energy of the nebular gas is of the order of the gravitational energy of the planet. Here M_p is the total mass of the planet, c_s is the isothermal sound speed, and \mathcal{R} is the reduced gas constant: $\mathcal{R} = k_b/(\mu m_p)$, with k_b the Boltzmann constant and m_p the proton mass. For $R_B < R_H$, several studies assume that the atmosphere matches onto the disk at R_B

(e.g., Ikoma et al. 2000, Pollack et al. 1996). One reason we always choose R_H as the matching radius is that, for hydrostatic solutions, the density at R_B is larger than the disk density by an order unity factor (Rafikov 2006). Additionally, even though gas flows no longer circulate the planet outside R_B , the density structure between R_B and R_H remains spherical and is still well described by hydrostatic balance (Ormel 2013), which justifies our outer boundary choice. At the Hill radius, the temperature and pressure are given by the nebular temperature and pressure: $T(R_H) = T_d$ and $P(R_H) = P_d$. We note, however, that we define the planet mass as the mass enclosed inside the smaller of R_B or R_H .

Lastly, we review the cooling model developed in Paper I used to determine the time evolution of the atmosphere between subsequent static models. A protoplanetary atmosphere embedded in a gas disk satisfies the following cooling equation:

$$L = L_c + \Gamma - \dot{E} + e_{\text{acc}} \dot{M} - P_M \frac{\partial V_M}{\partial t} \quad (6)$$

Here, L is the total luminosity, L_c is the luminosity from the solid core, which may include planetesimal accretion and radioactive decay, and Γ is the rate of internal heat generation. We set $L_c = \Gamma = 0$. The \dot{E} term is the rate at which total energy (internal and gravitational) is lost, e_{acc} is the specific total energy brought in by mass accreting at the rate \dot{M} : $e_{\text{acc}} = u - GM/R$, and the last term represents the work done on a surface mass element.

We obtain an evolutionary series for the atmosphere by connecting sets of subsequent static atmospheres through the cooling equation (6). Details of our numerical procedure are described in Paper I.

3. ADIABATIC GRADIENT FOR THE TABULATED EQUATION OF STATE

In order to describe the nebular gas, we use the interpolated EOS tables of Saumon et al. (1995) for a helium mass fraction $Y = 0.3$, and extend them to lower temperatures and pressures corresponding to the conditions in our fiducial disk. More details on our extension procedure and on the methodology of combining the separate tables for hydrogen and helium are presented in Appendix A.

For an ideal gas polytropic EOS, the adiabatic gradient is constant. In contrast, non-ideal effects such as dissociation or ionization produce temperature-dependent variations in ∇_{ad} . Figure 1 shows a contour plot of the adiabatic gradient (defined in equation 4) as a function of gas temperature and pressure. We distinguish three separate temperature regimes:

1. Intermediate temperature regime ($300 \text{ K} \lesssim T \lesssim 2000 \text{ K}$), where the hydrogen-helium mixture behaves like an ideal gas with a polytropic EOS.
2. High temperature regime ($T \gtrsim 2000 \text{ K}$), where dissociation of molecular hydrogen occurs, followed by ionization of atomic hydrogen for $T \gtrsim 10,000 \text{ K}$.
3. Low temperature regime ($T \lesssim 300 \text{ K}$), where the rotational states of the hydrogen molecule are not fully excited.

We note that helium behaves like an ideal monatomic gas with $\nabla_{\text{ad}} = 2/5$ in our regime of interest. Its presence in the atmosphere thus only causes a small, constant upper shift in the adiabatic gradient of the mixture.

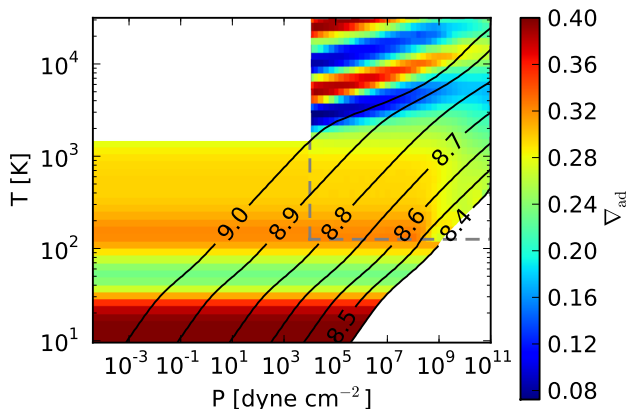


FIG. 1.— Contour plot of the adiabatic gradient ∇_{ad} for a hydrogen-helium mixture as a function of gas temperature and pressure. The upper-right rectangle encloses the region described by the original Saumon et al. (1995) EOS tables, while the rest of the plot is our extension. The black curves represent constant entropy adiabats, with the labels $\log_{10}(S)$ [erg K $^{-1}$ g $^{-1}$]. The regions in which the EOS is either invalid or not computed are masked in white. Our extension is only valid for $T \lesssim 2000$ K, since it does not take into account hydrogen dissociation. We choose $T = 1500$ K as a conservative temperature cutoff. Saumon et al. (1995) do not compute the EOS at very high pressures, since hydrogen is solid or may form a Coulomb lattice in this regime, and thus their EOS treatment is no longer valid. While the boundaries of the region in which the free-energy EOS treatment fails can be determined from fundamental thermodynamic constraints, such calculations are not the object of this work. Instead, we note that less pressure is needed for hydrogen to become solid at lower temperatures, and so we choose as boundary a constant entropy curve ($\log(S) = 8.4$) above the region in which the Saumon et al. (1995) model fails. The expressions derived in Appendix A are sufficient to give good results for the colored regions of the extended map, which fully cover the temperature and pressures ranges required by our models.

In what follows we explain the behavior of the adiabatic gradient in the three temperature regimes separately.

1. Intermediate T: Ideal Gas

For temperatures less than ~ 2000 K but larger than ~ 300 K, the hydrogen molecule is not energetic enough to dissociate and hydrogen behaves as an ideal diatomic gas. We see this in Fig. 1 for $300 \text{ K} \lesssim T \lesssim 3000 \text{ K}$, where the adiabatic gradient is approximately constant. The helium component of the gas causes a slight increase in the adiabatic index: $\nabla_{\text{ad}} \approx 0.3$ in this temperature range rather than $2/7$ as is the case for a diatomic gas¹.

2. High T: Dissociation and Ionization of Hydrogen.

At low temperatures, hydrogen exists in molecular form and has a stable configuration. As the temperature becomes higher than $T \sim 2000 - 3000$ K, the internal en-

ergy of the hydrogen molecule becomes large enough to break the covalent bond between the atoms, and hydrogen starts dissociating. Further energy increase at temperatures of $\sim 10^4$ K results in electrons being removed from atoms, i.e. hydrogen ionizes. In stellar and giant planet interiors there is little overlap between the two processes: hydrogen is almost entirely dissociated into atoms by the time ionization becomes important.

We see in Figure 1 that the adiabatic gradient decreases significantly in regions of partial dissociation and partial ionization. This behavior is different than that of a mixture of molecular and atomic hydrogen where $2/7 < \nabla_{\text{ad}} < 2/5$, or a mixture of protons and electrons where $\nabla_{\text{ad}} = 2/5$. We explain this in what follows.

For a mixture of ideal gases, the total internal energy is given by the sum of the internal energies of the individual gases. When a gas dissociates, however, part of the internal energy of the system is used to break down molecules, which reduces the amount of energy available to increase the temperature of the system, thus lowering the adiabatic gradient. The energy required to dissociate depends on the dissociation fraction, which can be determined from the Saha equation (see e.g., Kippenhahn & Weigert 1990). The dissociation fraction only depends on gas temperature and density, and hence only on the EOS.

An expression for the adiabatic gradient as a function of the dissociation fraction is presented in Appendix B. As expected, the adiabatic gradient is $\nabla_{\text{ad}} = 2/7$ for pure molecular hydrogen and $\nabla_{\text{ad}} = 2/5$ when hydrogen is fully dissociated, but decreases significantly during partial dissociation and is smallest when half of the gas is dissociated. This is consistent with the behavior we see in Figure 1.

The ionization of atomic hydrogen is also dictated by the Saha equation, with the dissociation energy replaced by ionization energy, hence the adiabatic gradient has an analogous behavior, consistent with Fig. 1.

3. Low T: Hydrogen Rotation and Spin Isomers

As a diatomic molecule, hydrogen has five degrees of freedom, three associated with translational motion and two associated with rotation. The excitation temperature for rotation is $\Theta_r \approx 85$ K for the hydrogen molecule (e.g., Kittel et al. 1981), hence the rotational states are fully excited at room temperature. As the gas temperature becomes comparable to Θ_r , fewer rotational states are excited and rotation entirely ceases as $T \rightarrow 0$.

Molecular hydrogen occurs in two isomeric forms, parahydrogen and orthohydrogen. Parahydrogen has antiparallel proton spins and thus an antisymmetric wave function. From the Pauli exclusion principle it follows that it can only occupy symmetric rotational states with even angular quantum number j (Farkas 1935). In contrast, orthohydrogen has parallel proton spins and a symmetric wave function, and can therefore only occupy states with odd j . At equilibrium, the relative abundance of the ortho- and para- states is given by the ratio of their partition functions, described in Appendix A. At $T \rightarrow 0$ all hydrogen molecules are in the ground state with $j = 0$, which corresponds to parahydrogen. As the temperature increases, parahydrogen starts converting into orthohydrogen, resulting in an ortho-para equilibrium ratio of

¹ Recall $\nabla_{\text{ad}} \equiv \frac{\gamma-1}{\gamma}$ for an ideal gas, with γ the adiabatic index: $\gamma = 7/5$ for a diatomic gas and $5/3$ for a monatomic gas.

3:1 at room temperature.

The adiabatic gradient scales as $\nabla_{\text{ad}} \sim 1/c_v = 1/(c_{v,t} + c_{v,r}) \sim 1/c_{v,r}$, with c_v the specific heat capacity at constant volume, and $c_{v,t}$ and $c_{v,r}$ the translational and rotational components, respectively. The second equality is due to the fact that $c_{v,t}$ is independent of temperature and equal to $3\mathcal{R}/2$. We can therefore understand the ∇_{ad} behavior by studying the dependence on temperature of $c_{v,r}$ of the ortho-para mixture.

The internal energy per unit mass and specific heat capacity associated with rotation for the individual isomers and for the equilibrium mixture can be derived from their partition functions (see Appendix A for details), and are plotted in Figure 2 (after Farkas 1935, Figure 1). At low temperatures, parahydrogen is in the $j = 0$ state and has no rotational energy, while orthohydrogen is in the $j = 1$ state and has the energy of its first rotational level. Both para- and orthohydrogen, as well as their equilibrium mixture, behave like monatomic gases at low temperatures and thus have zero rotational heat capacity. This is consistent with $\nabla_{\text{ad}} = 2/5$ at low temperatures as seen in Figure 1. As the temperature increases, the energetically higher-lying rotational states of para- and orthohydrogen are populated and the heat capacity of both spin isomers increases as a result. We note that the heat capacity of the equilibrium mixture is not a weighted average of the heat capacities of the individual components because it takes into account both the rotational energy uptake of para- and orthohydrogen, and also the shift in their equilibrium concentrations with temperature. This results in a peak in the heat capacity of the mixture around ~ 50 K, as seen in the bottom plot of Figure 2. As $\nabla_{\text{ad}} \sim 1/c_{v,r}$, it follows that the adiabatic gradient has to reduce, reach a minimum, then increase as the temperature rises, as shown in Figure 1.

4. EQUATION OF STATE EFFECTS ON ATMOSPHERE EVOLUTION

Variations in the adiabatic gradient ∇_{ad} due to partial dissociation and quantum rotational effects (see section §3) have two competing effects on the evolution of a core's atmosphere: (1) they yield a lower envelope luminosity, and (2) a larger amount of energy that needs to be radiated per unit mass, when compared to an ideal gas. Both effects combined slow down accretion and increase the growth time of the atmosphere, and therefore the crossover time and critical core mass.

In order to explain the quantum rotational effects at low temperatures, we make the following thought experiment: we imagine that realistic EOS effects only affect the upper atmosphere where temperatures are low, and that the gas is ideal and polytropic deep in the envelope. Conversely, we study the effects of dissociation at high temperatures by assuming that realistic EOS effects only matter at the bottom of the atmosphere where temperatures are high, and that the gas is polytropic in the outer regions. Figure 3 shows the time evolution of atmospheres forming at 10 AU around cores of mass $M_c = 10M_\oplus$ and described by various equations of state, as follows:

- Dashed curve (1) — ideal gas polytrope with $\nabla_{\text{ad}} = 0.3$.

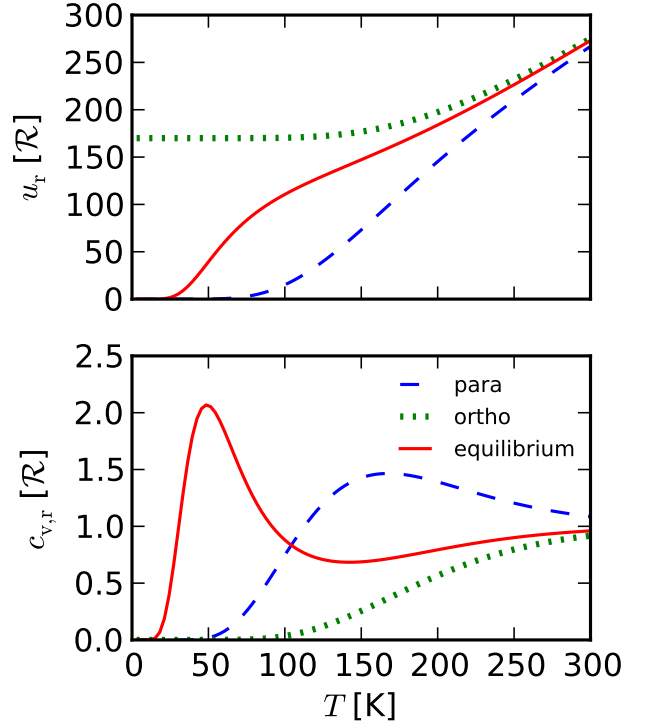


FIG. 2.— Internal energy per unit mass and specific heat capacity associated with rotation for parahydrogen (dashed blue), orthohydrogen (dotted green), and the equilibrium mixture (solids red) as a function of temperature. After Farkas (1935), Figure 1.

- Dotted curve (2) — ideal gas polytrope with $\nabla_{\text{ad}} = 0.3$ for $T > 500$ K and realistic EOS for $T < 500$ K.
- Dash-dotted curve (3) — ideal gas polytrope with $\nabla_{\text{ad}} = 0.3$ for $T < 500$ and realistic EOS for $T > 500$ K.
- Solid curve (4) — fully realistic EOS.

We choose $T = 500$ K as the cutoff temperature because the hydrogen-helium mixture behaves like an ideal gas, with $\nabla_{\text{ad}} = 0.3$, in this temperature regime (see Figure 1). As such, the difference in cooling times between curves (1) and (2) shows the quantum rotational effects on the atmosphere evolution, while the difference between curves (1) and (3) accounts for hydrogen dissociation. We see that both dissociation and rotational states have a comparable effect on the atmosphere growth and result in slower cooling. The cooling time is dependent on both the total energy released due to the contraction of the envelope and the luminosity of the atmosphere. We explore the relative influence of these two factors separately.

The upper-right panel of Figure 4 shows the luminosity evolution with mass for atmospheres (1)-(4), for an example core with $M_c = 10M_\oplus$ forming at 10 AU. We see that the lower luminosity of the fully realistic EOS (4) when compared to the polytrope (1) is due to the realistic EOS effects in the outer atmosphere (2). This behavior is directly correlated to the depth of the radiative region of the envelope, which is shown in the upper-left panel

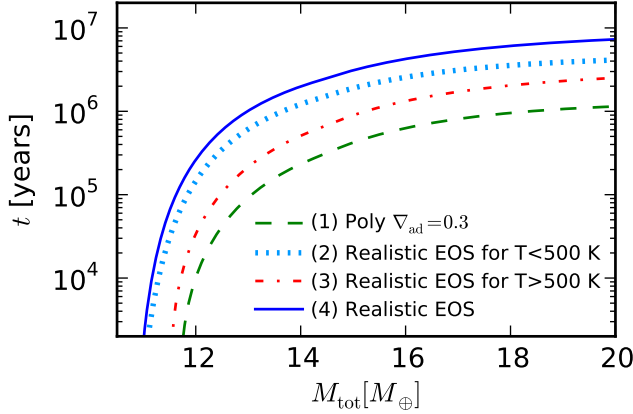


FIG. 3.— Elapsed time as a function of total mass (core + atmosphere) for a variety of EOS combinations (see text), for a planet forming at 10 AU and with a fixed core mass $M_c = 10M_\oplus$. Both hydrogen dissociation at high temperatures deep in the atmosphere and quantum rotational effects at low temperatures in the outer envelope result in slower cooling when compared to an ideal gas polytrope.

of Figure 4 for a total planet mass of $12M_\oplus$. We see that the realistic EOS for low temperatures (2) results in a deeper location of the RCB when compared to the ideal gas polytrope (1). This deeper RCB translates into a larger number of steps that photons need to diffuse to escape from the RCB, and therefore a lower luminosity (cf. equation 3). In fact, a simple estimate of the luminosity emerging at the RCB can be found as follows.

The equation of radiative diffusion (2c) can be approximated in terms of the radiative flux \mathcal{F} as

$$\mathcal{F} \sim \frac{\sigma T_{\text{RCB}}^4}{\tau}, \quad (7)$$

where τ is the optical depth of the upper radiative layer. Furthermore, we find that τ is dominated by the optical depth of the first scale height, i.e.

$$\tau \sim \tau_{\text{RCB}} = \kappa_{\text{RCB}} \rho_{\text{RCB}} H_{\text{RCB}}, \quad (8)$$

where

$$H_{\text{RCB}} = \frac{k_b T_{\text{RCB}}}{\mu m_H} \frac{R_{\text{RCB}}^2}{GM_{\text{RCB}}}, \quad (9)$$

with μ the mean molecular weight of the gas, m_H the proton mass, and all other quantities evaluated at the bottom of the radiative layer. By substituting equations (9) and (8) into equation (7), and noting that $\mathcal{F} = L/(4\pi(R_{\text{RCB}} + H_{\text{RCB}})^2) \approx L/(4\pi R_{\text{RCB}}^2)$, we recover equation (3) applied at the boundary between the uppermost convective region of the atmosphere and the outer radiative layer (where $\nabla_{\text{rad}} = \nabla_{\text{ad}}$).

Dissociation deep in the planet's atmosphere increases the amount of energy per unit mass that needs to be radiated by the envelope, which further slows down growth. Figure 4, lower-left plot, shows the total energy (internal and gravitational) profile as a function of the radial coordinate, for the same example planet. The bulk of the energy is concentrated deep in the atmosphere for the realistic EOS at high temperatures (3) and the fully realistic EOS curve (4), which shows that hydrogen dissoci-

ation in the inner atmosphere dictates the energy behavior of the envelope. In contrast, energy is concentrated towards the outer boundary for the $\nabla_{\text{ad}} = 0.3$ polytrope (1). Qualitatively, this can be explained through a simple analytic argument: the density profile in an adiabatic, non-self gravitating atmosphere composed of an ideal gas scales as $\rho(r) \sim r^{1/\nabla_{\text{ad}}-1}$ (see also Paper I). Since the energy per unit mass scales as $e(r) \sim \rho(r)r^2 \sim r^{1/\nabla_{\text{ad}}+1}$, it is easy to see that adiabats with lower adiabatic gradient have their energy more tightly packed towards the interior of the envelope, which is the case during dissociation when ∇_{ad} decreases significantly (see section §3 and Figure 1). It takes more energy to bring in gas deep in the atmosphere for an envelope that has the bulk of its energy concentrated towards the bottom, which increases the amount of energy per unit mass that needs to be radiated, i.e. $|dE/dM|$, and therefore the cooling time, for the realistic EOS at high temperatures (3) when compared to the ideal gas polytrope (1). This increase in $|dE/dM|$ is shown in the bottom-right panel of Figure 4.

We have seen that the quantum rotational effect at the outer boundary dictates the location of the radiative zone, and therefore the luminosity behavior, while dissociation deep in the atmosphere dictates the total energy behavior. Overall, both effects result in a longer time for the atmosphere to evolve.

5. CRITICAL CORE MASS

In this section we put together the results obtained in section §4 and determine the minimum core mass to initiate runaway gas accretion during the lifetime of the protoplanetary disk. As in Paper I, we define this minimum core mass as the *critical core mass*, and the time elapsed until runaway gas accretion is initiated when $M_{\text{atm}} \sim M_c$ as the *crossover time*. We first explore the dependence of the crossover time on the core mass for a fixed semi-major axis. We then determine the critical core mass to form a giant planet from a gas composed of a realistic hydrogen-helium mixture, and we compare this with the results from Paper I for an ideal diatomic gas. Finally, we determine the critical core mass under more realistic opacity assumptions.

Figure 5 displays the time evolution and the crossover time for atmospheres forming around cores with masses between $10 M_\oplus$ and $20 M_\oplus$ at $a = 10$ AU in our fiducial disk. The crossover time is shorter for higher mass cores, consistent with the results of Paper I.

Figure 6 shows the critical core mass for a massive atmosphere to form during a typical lifetime of a protoplanetary disk $t = 3$ Myrs (e.g., Jayawardhana et al. 1999), for a gas described by a realistic EOS and an ISM dust opacity given by equation 5. The results of Paper I for an ideal diatomic gas are plotted for comparison. The inclusion of realistic EOS effects results in a critical core mass more than twice as large than under the ideal gas assumption. As such, non-ideal effects substantially affect the core mass needed to form a giant planet before the dissipation of the protoplanetary disk.

The results above were obtained under the assumption that the dust opacity in the radiative region of the atmosphere is given by the standard ISM opacity (see also section §2.2). However, our scenario of low plan-

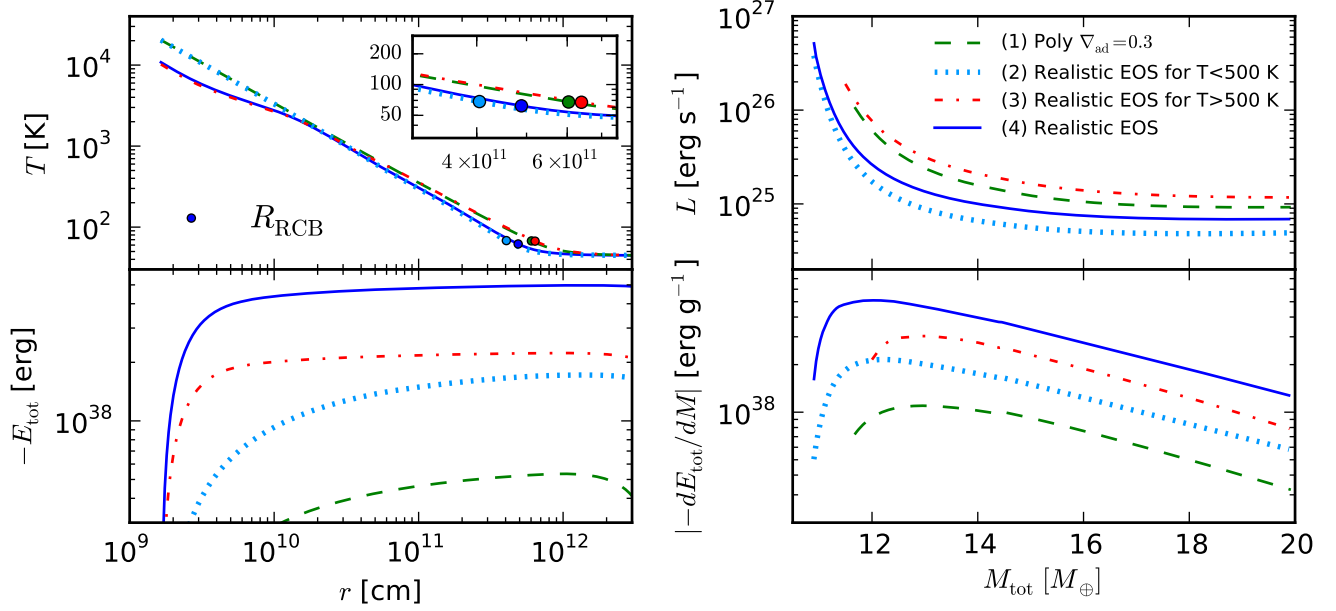


FIG. 4.— We explore atmosphere growth around a core of $M_c = 10M_\oplus$ forming at 10 AU in our fiducial disk, for the EOS choices in Figure 3. Upper-left panel: Instantaneous temperature profile for a total mass (core + atmosphere) of $12M_\oplus$ as a function of radius. The location of the RCB is marked. The quantum rotational effects at low temperatures in the outer region of the atmosphere dictate the location of the RCB. Upper-right panel: Luminosity evolution as a function of total mass (core + atmosphere). The quantum rotational effects at low temperatures near the top of the atmosphere result in a lower luminosity for the realistic EOS (see text). Lower-left panel: Instantaneous energy profiles as a function on radius for a total mass (core + atmosphere) of $12M_\oplus$. Hydrogen dissociation deep in the atmosphere causes the bulk of the energy to be concentrated at the bottom of the atmosphere. This increases the amount of energy per unit mass that needs to be radiated away, i.e. $|dE/dM|$, resulting in a longer crossover time for the realistic EOS when compared to the polytrope. Lower-right panel: $|dE/dM|$ evolution as a function of total mass (core + atmosphere). More energy per unit mass has to be radiated away due to hydrogen dissociation when compared to an ideal gas polytrope, which results in slower growth.

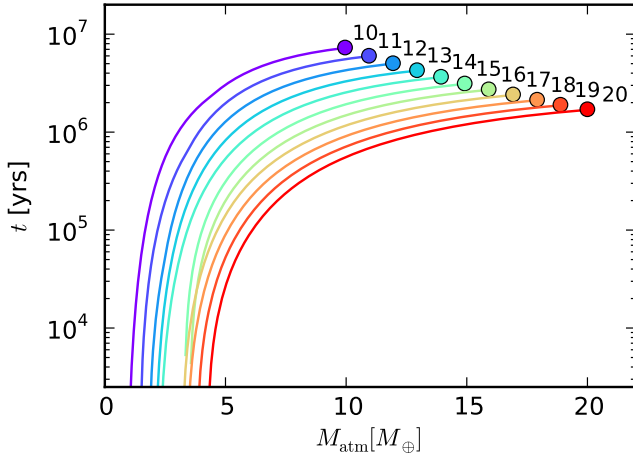


FIG. 5.— Elapsed time as a function of atmosphere mass, for cores with fixed masses between $10M_\oplus$ and $20M_\oplus$ at $a = 10$ AU in our fiducial disk. The circles mark the crossover time where $M_{\text{atm}} \sim M_c$. The numbers are labeling the core mass in Earth masses. A larger core mass results in a shorter crossover time.

etesimal accretion is likely to favor lower dust opacities, due to grain growth and dust settling. Grain growth, in particular, lowers the absolute value of the opacity and changes the particle size distribution when compared to the standard ISM size distribution (e.g., Pollack et al. 1985). **Didn't understand comment...**

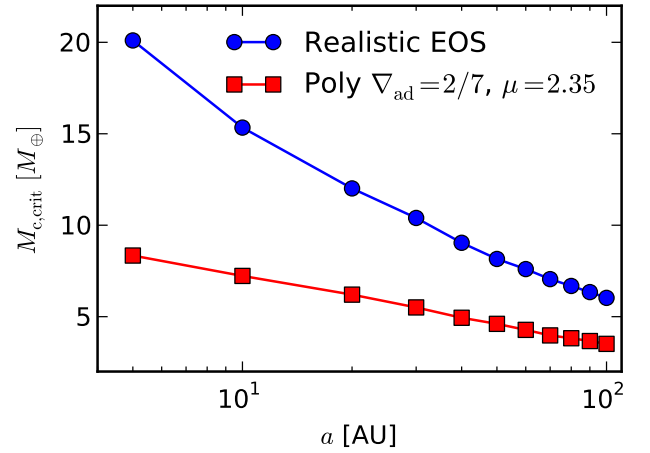


FIG. 6.— The minimum core mass for an atmosphere to initiate runaway gas accretion within the lifetime of a typical protoplanetary disk $t \sim 3$ Myrs as a function of semi-major axis, for a realistic hydrogen-helium mixture and a standard ISM power-law opacity. The results of Paper I for an ideal diatomic gas are plotted for comparison. The realistic equation of state yields core masses larger by more than a factor of 2 when compared to the polytrope.

Although grain growth and evidence for non-ISM size distribution have been observed in protoplanetary disks (e.g., Beckwith et al. 1990, Beckwith & Sargent 1991, Pérez et al. 2012), the size distribution of dust particles has not been tightly constrained. Typically, the grain

size distribution is assumed to be a power law:

$$n \sim a^{-p}, \quad (10)$$

where a is the particle radius and $p = 3.5$ (corresponding to a “normal” collisional cascade) or $p = 2.5$ (an approximation for coagulation). In this work we use the D’Alessio et al. (2001) frequency-dependent opacity tables to obtain the temperature-dependent Rosseland mean opacity κ , assuming a maximum particle size of 1 cm and a grain size distribution given by equation (10) with $p = 3.5$ as a fiducial case. Other choices for the power-law coefficient p are discussed later in this section.

The D’Alessio et al. (2001) opacities are only relevant at temperatures that are sufficiently low for dust grains to remain solid ($T \lesssim 1000$ K). In the temperature regime where dust sublimates we use the Bell & Lin (1994) analytic opacity laws, ensuring smooth transition from the grain growth opacities.

The sharp drop in opacity ($\kappa \sim T^{-24}$) due to dust sublimation lowers the radiative temperature gradient significantly (see equation 3), and may therefore generate radiative layers within the inner region of the atmosphere (see Appendix C, Figure 15). This could in principle pose challenges for our model, since the additional luminosity generated in these radiative windows may be large enough to make our assumption of constant luminosity throughout the radiative layers invalid. In practice, however, the inner radiative windows are either very thin (Figure 15, middle panel), or the temperature gradient is flat enough to result in a roughly constant luminosity throughout the region (Figure 15, bottom panel; also see equation 2c). This results in a negligible extra luminosity generated in the radiative windows. While the above is true for our fiducial opacity law, the radiative windows may become non-negligible for other opacity choices and sufficiently low core masses, as we show later in this section. We note that despite the existence of one or more radiative windows in the planet atmosphere, the luminosity that emerges at the outer boundary is set by the top radiative window, as is the case for the standard inner convective-outer radiative envelopes.

Due to the variable number and position of radiative windows, and therefore radiative-convective boundaries, within the planet atmosphere, we cannot consistently calculate the time evolution of different atmospheres if we evaluate our cooling equation (6) at the RCB, as we do in our standard model. We choose to evaluate the cooling time at the Bondi radius instead (since our cooling model applies at any radius R , see section §2.2). We note that our choice of \bar{R} does not change the estimate of the atmosphere evolution time, to order of magnitude, since the additional luminosity generated in all radiative regions is negligible for our opacity choice (also see Paper I).

Figure 7 shows the resulting critical core mass as a function of semi-major axis. The critical core mass is lower than in the standard case, and less sensitive to the distance in the disk, i.e. the boundary conditions (temperature and pressure). We have shown in Paper I that the critical core mass is highly dependent on disk temperature rather than pressure. The temperature dependence, however, is mainly due to opacity: for the simplified analytic model developed in Paper I we found that

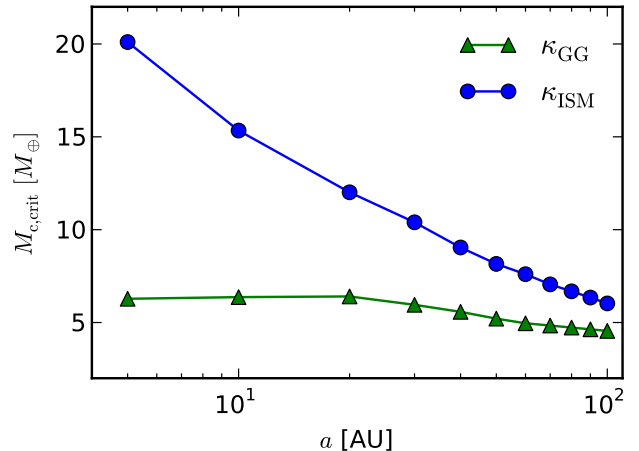


FIG. 7.— Critical core mass as a function of semi-major axis for radiative opacities that account for grain growth. The critical core mass is lower than in our fiducial case where dust grains have a standard ISM distribution.

the crossover time $t_{co} \sim T^{\beta+1/2}$, with β the power-law exponent in equation (5). Opacity is less sensitive to temperature variations for larger grains and has an almost flat profile (see Figure 14), which results in $\beta \ll 1$ and a much weaker temperature (and therefore semi-major axis) dependence of the critical core mass, as seen in Figure 7. Moreover, grain growth reduces the absolute value of the opacity, which results in an overall lower crossover time and critical core mass.

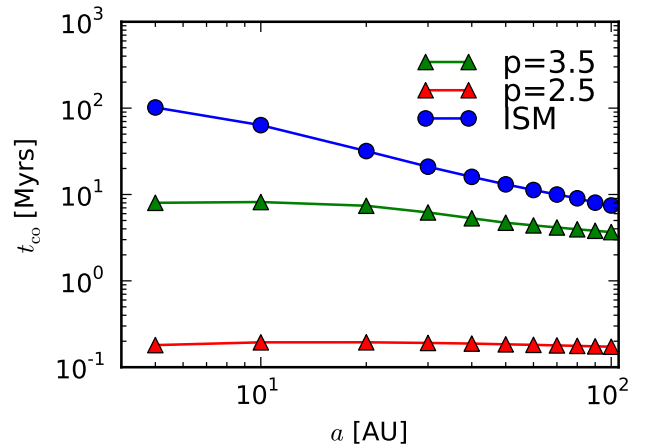


FIG. 8.— Crossover time for different grain size distribution, for a planet forming around a core $M_c = 4M_\oplus$. The standard ISM result is plotted for comparison. The crossover time is more than one order of magnitude lower when coagulation is accounted for, i.e. $p = 2.5$.

In our calculation so far we assumed that the size distribution of dust grains is the power law (10) with $p = 3.5$, which corresponds to a normal collisional cascade. If, however, coagulation is taken into account, the exponent p can be approximated as $p = 2.5$ (D’Alessio et al. 2001). This results in a flatter and significantly lower opacity, which may substantially reduce the critical core mass.

However, we have found that our model breaks down for low core masses ($M_c \lesssim 3M_\oplus$) under this assumption, i.e. the outer radiative region becomes deep enough that the luminosity generated in this region can no longer be neglected. Figure 8 shows the crossover time as a function of semi-major axis for the lowest core mass in which our model is valid, $M_c = 4M_\oplus$. The crossover time is more than one order of magnitude lower when coagulation is accounted for, which implies that the critical core mass may be, in fact, significantly lower than presented in Figure 7.

6. EFFECTS OF PLANETESIMAL ACCRETION

In this study we have considered protoplanets with fully formed cores for which planetesimal accretion is negligible and KH contraction dominates the luminosity evolution of the atmosphere. This is different from calculations that assume high planetesimal accretion rates and find that the atmosphere is in steady state and solely heated due to accretion of solids. In this section we compare our results for the critical core mass to analogous results from steady-state analytic calculations. We discuss the core accretion rates that are necessary for our regime to be valid in section §6.1. In section §6.2, we estimate core growth during atmosphere evolution at the maximum rate for which the KH regime is valid, and show it is negligible. Finally, we compare our results with those assuming fast planetesimal accretion in section §6.3.

6.1. Planetesimal Accretion Rates

Kelvin-Helmholtz contraction dominates an atmosphere's luminosity if $L_{acc} < L_{KH}$, where L_{acc} is the accretion luminosity,

$$L_{acc} = G \frac{M_c \dot{M}_c}{R_c}, \quad (11)$$

and K_{KH} is given by equation (6) with $L_c = \Gamma = 0$ (see section 2.2). This condition is satisfied as long as the planetesimal accretion rate

$$\dot{M}_c < \dot{M}_{c,KH} \equiv \frac{L_{KH} R_c}{GM_c}. \quad (12)$$

To calculate $\dot{M}_{c,KH}$, we choose as a fiducial case an atmosphere forming at 10 AU and with a core mass of $10M_\oplus$. Since analytic studies assume an ideal gas EOS, for ease of comparison we choose an ideal gas polytrope with constant adiabatic gradient $\nabla_{ad} = 2/7$ and mean molecular weight $\mu = 2.35$ (see also Paper I). For this choice of parameters, the atmosphere crossover time is $t_{co} \sim 1.2$ Myrs, which is within the typical lifetime of a protoplanetary disk. The results are presented in Figure 9. The atmosphere growth rate \dot{M}_{atm} is also plotted for comparison. We see that the core accretion rate has to be $\sim 2 - 3$ orders of magnitude lower than the atmosphere accretion rate for our assumptions to be valid. If the core had accreted planetesimals at the $\dot{M}_{c,KH}$ rate since it started forming, it couldn't have grown large enough to attract an atmosphere within typical disk lifetime. This is consistent with the requirement of our model that the planetesimal accretion rate is initially large during core growth, then significantly reduces as the gaseous envelope accumulates. This is a plausible scenario, as the

core may have formed in the inner part of the disk and was later scattered outwards (Ida et al. 2013), or the planet's feeding zone could have been depleted of solids due to a giant neighbor. We further estimate two reference accretion rates. The first one is the core accretion rate $\dot{M}_{c,acc}$ needed to grow the core to $M_c = 10M_\oplus$ on the same timescale as our model atmosphere, $\tau = 1.2$ Myrs:

$$\dot{M}_{c,acc}(M_c) \equiv \frac{M_c}{\tau}. \quad (13)$$

The second reference planetesimal accretion rate is $\dot{M}_{c,Hill}$, a typically assumed planetesimal accretion rate for which the random velocities of the planetesimals are of the order of the Hill velocity around the protoplanetary core (for a review, see Goldreich et al. 2004). This is the accretion rate at the boundary between the dispersion dominated and shear dominated regimes. Following Rafikov (2006) (equation A1),

$$\dot{M}_{c,Hill} = \Omega \Sigma_p R_c R_H, \quad (14)$$

where Σ_p is the surface density of solids, assumed to satisfy $\Sigma_d \approx 100\Sigma_p$ for a dust-to-gas ratio of 0.01.

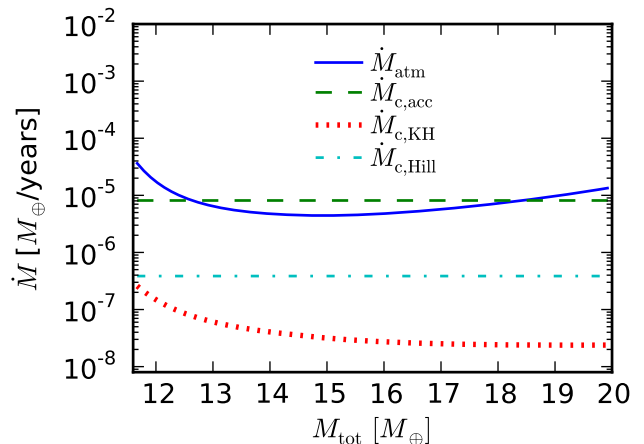


FIG. 9.— Various accretion rates in the case of a planet forming at 10 AU and with a core mass $M_c = 10M_\oplus$, for a polytropic EOS and ISM power-law opacity. For this choice of parameters, the crossover time (defined in section §5) is $t_{co} \sim 1.2$ Myrs. The \dot{M}_{atm} (solid blue) curve represents the growth rate of the atmosphere as estimated by our model, and $\dot{M}_{c,KH}$ (dotted red) is the maximum planetesimal accretion rate during the gas contraction phase in order for our regime to be valid, i.e. $L_{acc} < L_{KH}$ (see text). For comparison, we plot the core accretion rate $\dot{M}_{c,acc}$ (dashed green) necessary to grow the core on a timescale $\tau = t_{co}$, and a typically assumed planetesimal accretion rate $\dot{M}_{c,Hill}$ (dash-dotted light blue) for which the random velocity of the planetesimals is given by the Hill velocity due to the core (see text). We note that $\dot{M}_{c,KH}$ and $\dot{M}_{c,Hill}$ are both lower than $\dot{M}_{c,acc}$, consistent with our assumptions that planetesimal accretion must have slowed down after core growth.

6.2. Core Growth during KH Contraction

In this section we investigate whether planetesimal accretion during the gas contraction phase at the rate $\dot{M} < \dot{M}_{c,KH}$ can alter the core mass enough to affect the

time evolution of the atmosphere. We can quantitatively estimate the increase in core mass as

$$\Delta M_c = \int_0^{t_{co}} \dot{M}_c dt \approx \sum_i \dot{M}_{ci} \Delta t_i, \quad (15)$$

where the accretion rate \dot{M}_{ci} is given by

$$\dot{M}_{ci} = \frac{L_i R_c}{GM_c} \quad (16)$$

from equation (11), with L_i the luminosity of the atmosphere at time t_i in our model. For $M_c = 10M_\oplus$, we find $\Delta M_c \approx 0.2M_\oplus \ll 10M_\oplus$. It follows that a significant increase in core mass that could potentially alter the time evolution of the atmosphere would occur on a much longer timescale than the crossover time for the unperturbed atmosphere. The time evolution of the atmosphere is thus insensitive to core mass changes at a rate imposed by the assumption that $L_{acc} < L_{KH}$.

6.3. Comparison with Steady-State Results

Next, we check that runaway gas accumulation due to planetesimal accretion cannot already commence before the atmosphere becomes unstable due to KH contraction, as our regime is no longer relevant under such conditions. We recall that in steady-state studies, the critical core mass is the maximum core mass for which the atmosphere is still in hydrostatic balance; runaway gas accumulation occurs if the core mass grows further. A higher planetesimal accretion rate results in a larger critical core mass for the steady-state models. As such, if unstable atmosphere collapse does not occur due to planetesimal accretion for the lowest value of $\dot{M}_{c,KH}$ over the course of the atmosphere's growth (see, e.g., Figure 9), then it can only occur in the KH dominated regime. In what follows we calculate the critical core mass $M_{crit,KH}$ corresponding to $\min(\dot{M}_{c,KH})$ and show that it is higher than the critical core mass we determined in the KH dominated regime.

In order to estimate $M_{crit,KH}$, we use the results of Rafikov (2006) for low luminosity atmospheres forming in the outer disk ($> 2-5$ AU), consistent with our region of interest. Rafikov (2006) assumes an ideal gas polytropic EOS and a lower opacity than the standard ISM opacity that we use in our calculations (see equation 5). We thus calculate the critical core mass for an ideal gas polytrope with the normalization factor F_κ reduced by a hundred, which is comparable to the opacity law used by Rafikov (2006)².

Following Rafikov (2006), we find the following expression for the critical core mass when accretion luminosity dominates the evolution of the atmosphere:

$$M_{crit,KH} \sim \left[\frac{\min[\dot{M}_{c,KH}(M_c)]}{64\pi^2 C} \frac{\kappa_0}{\sigma G^3} \frac{1}{R_c M_c^{1/3}} \left(\frac{k_b}{\mu} \right)^4 \right]^{3/5}, \quad (17)$$

² The power-law opacity of Rafikov (2006) is scaled to the (semi-major axis dependent) disk temperature, while our opacity is scaled to an absolute reference temperature. We thus cannot directly use the Rafikov (2006) opacities for our comparison.

with C an order unity constant depending on the adiabatic gradient and disk properties (see Rafikov 2006, equation B3). From equation (12), the accretion rate $\dot{M}_{c,KH}$ depends on the core mass M_c . We find $M_{crit,KH}$ numerically by setting $M_c = M_{crit,KH}$ on the right-hand side of equation (17). The result is displayed in Figure 10; the critical core mass corresponding to planetesimal accretion at the rates displayed in Figure 9 is displayed for comparison.

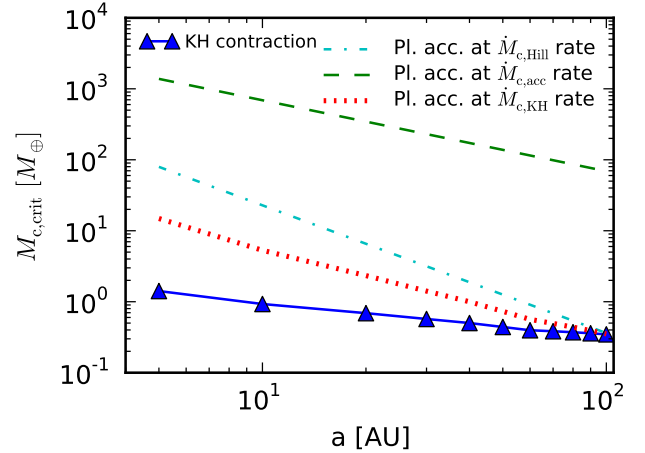


FIG. 10.— Comparison between the critical core mass $M_{crit,KH}$ due to planetesimal accretion and the assumed fixed core mass when gas contraction dominates. Our results yield lower core masses than in the fast planetesimal accretion case (e.g., Rafikov 2006). The critical core mass corresponding to $\dot{M}_{c,Hill}$ and $\dot{M}_{c,acc}$ from Figure 9 is plotted for comparison.

The critical core mass due to KH contraction is smaller than in the case in which planetesimal accretion dominates the evolution of the atmosphere. This brings us to two conclusions. First, we confirm that planetesimal accretion can be safely ignored in our regime of interest. Secondly, this comparison tells us that the core mass needed to form a giant planet is smaller if the core forms first, then accretes a massive envelope, than in the case where the core and atmosphere grown simultaneously in a high planetesimal accretion regime. Moreover, our result represents a true, absolute minimum on the core mass needed to form a giant planet during the lifetime of the protoplanetary disk, as our core no longer grows.

7. CONCLUSIONS

In this paper we study the formation of giant planets embedded in a gas disk. We consider atmosphere evolution around fully grown cores and determine the minimum (critical) core mass required to form a gas giant during the typical lifetime of a protoplanetary disk. We improve the model developed in Paper I (**does this also need to be written out as Piso & Youdin?**) by including realistic equation of state (EOS) tables and dust opacities. For a realistic EOS and interstellar grain opacity, the critical core mass is $\sim 20M_\oplus$ at 5 AU and drops to $\sim 6M_\oplus$ in our fiducial disk. These results are more than twice as large than those calculated in Paper I for a polytropic EOS, and bring the critical core mass to

$\sim 10M_{\oplus}$, the value typically quoted in many core accretion studies. When realistic opacities that include grain growth are used, the critical core mass is significantly lower, i.e. $\sim 6M_{\oplus}$ at 5 AU and $\sim 4M_{\oplus}$ at 100 AU. Different assumptions about the grain size distribution (e.g., that take into account coagulation) may further reduce the critical core mass.

Our results yield lower core masses than analogous results that consider high planetesimal accretion rates for which the core and atmosphere grow simultaneously. It

is thus possible to form a giant planet from a smaller core if the core grows first, then the accretion rate of solids is reduced and a gaseous envelope is accumulated. Moreover, since additional heat sources such as planetesimal accretion limit the ability of the atmosphere to cool and undergo Kelvin-Helmholtz contraction, our results represent a true minimum on the core mass needed to form a giant planet during the typical lifetime of a protoplanetary disk.

REFERENCES

- Beckwith, S. V. W. & Sargent, A. I. 1991, *ApJ*, 381, 250
 Beckwith, S. V. W., Sargent, A. I., Chini, R. S., & Guesten, R. 1990, *AJ*, 99, 924
 Bell, K. R. & Lin, D. N. C. 1994, *ApJ*, 427, 987
 Blanksby, S. J. & Ellison, G. B. 2003, *Acc. Chem. Res.*, 36, 255
 Bodenheimer, P. & Pollack, J. B. 1986, , 67, 391
 Chiang, E. & Youdin, A. N. 2010, *Annual Review of Earth and Planetary Sciences*, 38, 493
 D'Alessio, P., Calvet, N., & Hartmann, L. 2001, *ApJ*, 553, 321
 D'Angelo, G., Durisen, R. H., & Lissauer, J. J. *Giant Planet Formation*, ed. S. Piper, 319–346
 Farkas, A. 1935, *Orthohydrogen, Parahydrogen and Heavy Hydrogen*
 Goldreich, P., Lithwick, Y., & Sari, R. 2004, *ARA&A*, 42, 549
 Ida, S., Lin, D. N. C., & Nagasawa, M. 2013, *ApJ*, 775, 42
 Ikoma, M., Nakazawa, K., & Emori, H. 2000, *ApJ*, 537, 1013
 Jayawardhana, R., Hartmann, L., Fazio, G., Fisher, R. S., & Telesco, C. M., & Piña, R. K. 1999, *ApJ*, 521, L129
 Kippenhahn, R. & Weigert, A. 1990, *Stellar Structure and Evolution*
 Kittel, C., Kroemer, H., & Landsberg, P. T. 1981, *Nature*, 289, 729
 Langmuir, I. 1912, *J. Am. Chem. Soc.*, 34, 860
 Mandl, F. 1989, *Statistical Physics*, 2nd Edition
 Mizuno, H., Nakazawa, K., & Hayashi, C. 1978, *Progress of Theoretical Physics*, 60, 699
 Ormel, C. W. 2013, *MNRAS*, 428, 3526
 Papaloizou, J. C. B. & Nelson, R. P. 2005, *A&A*, 433, 247
 Papaloizou, J. C. B. & Terquem, C. 1999, *ApJ*, 521, 823
 Pérez, L. M., Carpenter, J. M., Chandler, C. J., Isella, A., Andrews, S. M., Ricci, L., Calvet, N., Corder, S. A., Deller, A. T., Dullemond, C. P., Greaves, J. S., Harris, R. J., Henning, T., Kwon, W., Lazio, J., Linz, H., Mundy, L. G., Sargent, A. I., Storm, S., Testi, L., & Wilner, D. J. 2012, *ApJ*, 760, L17
 Pollack, J. B., Hubickyj, O., Bodenheimer, P., Lissauer, J. J., Podolak, M., & Greenzweig, Y. 1996, , 124, 62
 Pollack, J. B., McKay, C. P., & Christofferson, B. M. 1985, , 64, 471
 Rafikov, R. R. 2006, *ApJ*, 648, 666
 Saumon, D., Chabrier, G., & van Horn, H. M. 1995, *ApJS*, 99, 713
 Semenov, D., Henning, T., Helling, C., Ilgner, M., & Sedlmayr, E. 2003, *A&A*, 410, 611
 Stevenson, D. J. 1982, *Planet. Space Sci.*, 30, 755
 Thompson, M. J. 2006, *An introduction to astrophysical fluid dynamics*
 Vardya, M. S. 1960, *ApJS*, 4, 281

APPENDIX

EQUATION OF STATE TABLES

In this study we consider atmosphere growth in the outer parts of protoplanetary disks ($a \lesssim 100$ AU), where temperature and pressure drop to $T \sim 20$ K and $P \sim 10^{-4}$ dyn cm $^{-2}$ for our MMSN disk model (see equations 1b and 1c). We assume that the nebular gas is described by a realistic equation of state (EOS), as prescribed by the Saumon et al. (1995) EOS tables. However, these tables only cover a relatively high range of temperatures and pressures, i.e. $2.1 < \log_{10} T(\text{K}) < 7.06$ and $4.0 < \log_{10} P(\text{dyn cm}^{-2}) < 19.0$. We thus need to extend the tables to lower T and P , as required by our disk model. We choose $\log_{10} T = 1.0$ and $\log_{10} P = -4.4$ as our lower boundaries for temperature and pressure, respectively, resulting in an extended temperature and pressure grid

$$1.0 < \log_{10} T < 2.1, \quad (\text{A1})$$

$$-4.4 < \log_{10} P < 4.0. \quad (\text{A2})$$

$$(\text{A3})$$

The other thermodynamic variables in the tables are calculated as follows.

Hydrogen

For a system of particles, the partition function can be written as the product of all partition functions associated with each type of energy that the system can have:

$$Z = Z_t Z_r Z_v \quad (\text{A4})$$

where Z_t , Z_r , Z_v are the partition functions associated with translation, rotation, and vibration, respectively³. Our derivations follow Kittel et al. (1981)

In the classical limit, the partition function associated with the motion of the center of mass of a gas molecule of mass m is given by:

$$Z_t = (m/2\beta\pi\hbar^2)^{3/2} V, \quad (\text{A5})$$

³ We ignore electronic and nuclear excitation as they are only

important at temperatures much higher than our regime of interest

with T and V the gas temperature and volume, respectively, \hbar the reduced Planck constant, and $\beta = 1/(k_b T)$. The rotational partition function is generally written as:

$$Z_r = \sum_{j=0}^{\infty} (2j+1) \exp \left[\frac{-j(j+1)\Theta_r}{T} \right], \quad (\text{A6})$$

where Θ_r is the characteristic temperature for rotational motion. In the case of hydrogen, $\Theta_r \approx 85$ K. However, molecular hydrogen occurs in two isomeric forms: orthohydrogen, with the proton spins aligned parallel to each other, and parahydrogen, with the proton spins aligned antiparallel. Parahydrogen can only have symmetric (even) wave function associated with rotation, while orthohydrogen can only have an antisymmetric (odd) wave function associated with rotation (see section §3 for an explanation why). The rotational partition functions for ortho- and parahydrogen can thus be written as:

$$Z_{r,\text{para}} = \frac{1}{2} \sum_{j=0}^{\infty} (1 + (-1)^j)(2j+1) \exp \left[-\frac{j(j+1)\Theta_r}{T} \right] \quad (\text{A7})$$

and

$$Z_{r,\text{ortho}} = \frac{3}{2} \sum_{j=0}^{\infty} (1 - (-1)^j)(2j+1) \exp \left[-\frac{j(j+1)\Theta_r}{T} \right] \quad (\text{A8})$$

The factor of 3 above accounts for the three-fold degeneracy of the ortho state.

When the two isomers are in equilibrium, the combined partition function is given by the sum of the individual partition functions, $Z_r = Z_{r,\text{ortho}} + Z_{r,\text{para}}$ and can be written as:

$$Z_r = \sum_{j=0}^{\infty} (2 - (-1)^j)(2j+1) \exp \left[\frac{-j(j+1)\Theta_r}{T} \right] \quad (\text{A9})$$

In our range of temperatures of interest, we found that Z_r converges after about 25 terms in the series.

Finally, the partition function for vibrational motion is given by:

$$Z_v = [1 - \exp(\theta_v/T)]^{-1}, \quad (\text{A10})$$

where θ_v is the characteristic temperature for vibrational motion, $\theta_v \approx 6140$ K for hydrogen.

If the partition function of a system particles is known in terms of (V, T) , the internal energy per unit mass, entropy per unit mass and specific heat capacity can be written as

$$U = \mathcal{R}T^2 \left(\frac{\partial \log Z}{\partial T} \right)_V \quad (\text{A11})$$

$$S = \mathcal{R} \log Z + \frac{U}{T} \quad (\text{A12})$$

$$C_v = \left(\frac{\partial U}{\partial T} \right)_V. \quad (\text{A13})$$

Since $Z = Z_t Z_r Z_v$, it is easy to notice that $U = U_t + U_r + U_v$ and $S = S_t + S_r + S_v$, where U_t , U_r , U_v , S_t , S_r , S_v are the quantities corresponding to the individual translation, rotation and vibration partition functions, respectively.

The entropy per mass due to translational motion can be expressed as:

$$S_t = \mathcal{R} \left[\frac{5}{2} \ln T - \ln P + \ln \left(\frac{(2\pi)^{3/2} \mathcal{R}^{5/2} \mu^4}{h^3} \right) + \frac{5}{2} \right] \quad (\text{A14})$$

with μ the mean molecular weight. Equation (A14) is known as the Sackur-Tetrode formula, and it is only applicable to an ideal gas. The internal energy per mass due to translational motion is given by:

$$U_t = \frac{3}{2} \mathcal{R}T \quad (\text{A15})$$

Putting all of the above together, we can now evaluate the thermodynamic quantities needed to extend the Saumon et al. (1995) EOS tables to low temperatures and pressures.

1. **Density.** In the low temperature, low pressure regime, hydrogen is molecular and behaves like an ideal gas. As such, the density in this region follows the ideal gas law $P = \rho \mathcal{R}T$.
2. **Internal energy per mass.** $U = U_t + U_r + U_v$, where U_t is given by equation (A15), and U_r , U_v are determined using equations (A11), (A9) and (A10) above.

3. **Entropy per unit mass.** Similarly, $S = S_t + S_r + S_v$, where S_t is given by equation (A14), and S_r , S_v can be determined from equation (A12) and the calculated expressions for U_r and U_v , respectively.
4. **Entropy logarithmic derivatives.** The logarithmic derivatives S_T and S_P are given by:

$$S_T = \left. \frac{\partial \log S}{\partial \log T} \right|_P \quad (\text{A16})$$

and

$$S_P = \left. \frac{\partial \log S}{\partial \log P} \right|_T \quad (\text{A17})$$

We calculate S_T and S_P through finite differencing.

5. **Adiabatic gradient ∇_{ad} .** The adiabatic gradient is defined as:

$$\nabla_{\text{ad}} = \left. \frac{\partial \log T}{\partial \log P} \right|_S = -\frac{S_P}{S_T} \quad (\text{A18})$$

We evaluate it from the tabulated values for S_T and S_P determined above. Figure 11 shows a contour plot of ∇_{ad} as a function of temperature and pressure for the extended EOS table.

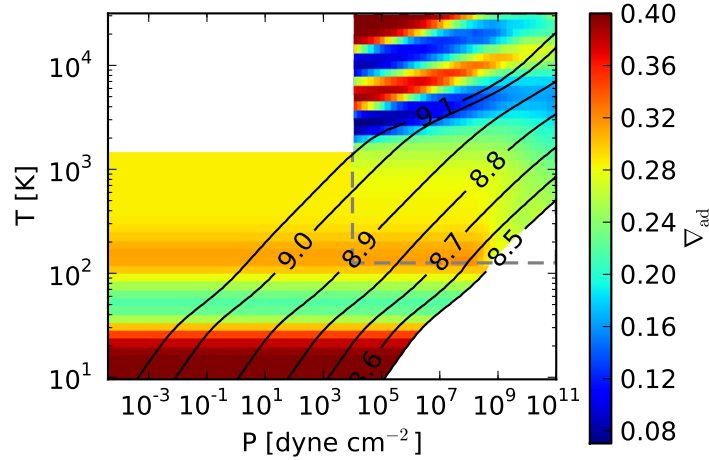


FIG. 11.— Contour plot of the hydrogen adiabatic gradient ∇_{ad} as a function of gas temperature and pressure. The upper right rectangle encloses the region described by the original Saumon et al. (1995) EOS tables, while the rest of the plot is our extension to lower temperatures and pressures. The black curves represent constant entropy adiabats, with the labels the natural logarithm of the absolute entropy per unit mass. At high temperatures, hydrogen dissociates and ionizes, while at low temperatures the rotational states of the hydrogen molecule are only partially excited and it no longer behaves like an ideal diatomic gas. Regions in which the EOS is invalid or has not been computed are masked in white (see Figure 1 caption for an explanation).

Helium

We extend the helium EOS tables based on a similar procedure. Since helium is primarily neutral and atomic at low temperatures and pressures, we treat it as an ideal monoatomic gas, and thus only take into account the translational component of the partition function (A5). Figure 12 shows ∇_{ad} as a function of temperature and pressure for the extended EOS table.

Lastly, we obtain the equation of state tables for the hydrogen-helium mixture thorough the procedure described in Saumon et al. (1995), for a helium mass fraction $Y = 0.3$.

ADIABATIC GRADIENT DURING PARTIAL DISSOCIATION

The total internal energy of a partially dissociated gas includes contributions from the individual internal energies of the molecules and atoms, as well as from the dissociation energy. The dissociation energy depends on the dissociation fraction x (i.e., the fraction of molecules that have dissociated), which can be found from the Saha equation (see e.g., Kippenhahn & Weigert 1990, Chapter 14) as a function of temperature and density,

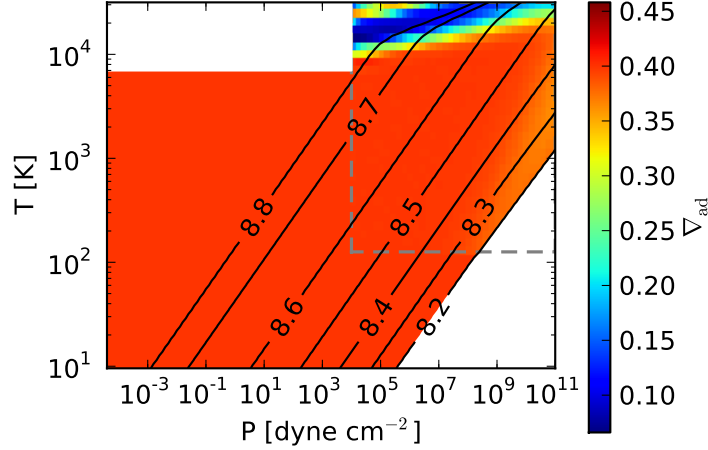


FIG. 12.— Contour plot of the helium adiabatic gradient ∇_{ad} as a function of gas temperature and pressure. The upper right rectangle encloses the region described by the original Saumon et al. (1995) EOS tables, while the rest of the plot is our extension to lower temperatures and pressures. The black curves represent constant entropy adiabats, with the labels the natural logarithm of the absolute entropy per unit mass. Helium ionizes at $T \gtrsim 10,000$ K, but behaves as an ideal monatomic gas otherwise. We choose $T = 7,000$ K as a conservative temperature cutoff above which our extension is no longer valid (masked in white). The EOS has not been computed in the lower-right region of the plot — see Figure 1 for an explanation.

$$\frac{x^2}{1-x} \propto \frac{T^{3/2}}{\rho} e^{-\chi/k_B T}, \quad (\text{B1})$$

with χ the dissociation energy, equal to 4.48 eV for molecular hydrogen (Blanksby & Ellison 2003).

The above also holds true for ionization, with the dissociation energy replaced by ionization energy $\chi = 13.6$ eV for atomic hydrogen (Mandl 1989). From the Saha equation one can find an expression for ρ as a function of T and x , then derive the adiabatic gradient directly from its definition (equation 4), taking into account the fact that the mean molecular weight in the ideal gas law varies with x , hence the pressure will not only be a function of T and ρ but also of x (see Kippenhahn & Weigert 1990, Chapter 14.3 for a detailed derivation). The final expression for the adiabatic gradient during ionization is

$$\nabla_{\text{ad}} = \frac{2 + x(1-x)\Phi_H}{5 + x(1-x)\Phi_H^2}, \quad (\text{B2})$$

with $\Phi_H \equiv \frac{5}{2} + \frac{\chi}{k_B T}$. The derivation of ∇_{ad} during dissociation is more involved mathematically (see, e.g., Vardya 1960) and leads to a slightly more complicated final expression,

$$\nabla_{\text{ad}} = \frac{1 + x + \frac{x(1-x^2)}{2} \frac{\chi}{k_B T}}{5x + \frac{7(1-x)}{2} + \frac{x(1-x^2)}{2} \left(\frac{\chi}{k_B T} \right)^2}. \quad (\text{B3})$$

We recover $\nabla_{\text{ad}} = 2/7$ for $x = 0$ (no ongoing dissociation hence hydrogen is purely molecular and diatomic) and $\nabla_{\text{ad}} = 2/5$ for $x = 1$ (hydrogen is fully dissociated into atoms and hence monatomic). Figure 13 shows the dependence of ∇_{ad} on the dissociation fraction, for $T = 3000$ K, the temperature at which dissociation typically occurs (Langmuir 1912). The adiabatic gradient drops substantially during partial dissociation, since part of the internal energy is used in dissociation rather than in increasing the temperature of the system.

GRAIN GROWTH OPACITY AND RADIATIVE WINDOWS

The opacity of the interstellar medium is reasonably well constrained and approximate analytic expressions for the Rosseland mean opacity as a function of temperature and density are derived in Bell & Lin (1994). For low temperatures ($T \lesssim 100$ K) at which ice grains are present, opacity scales with temperature as $\kappa \sim T^2$. Sublimation of ice grains at ~ 150 K and of metal grains at ~ 1000 K results in sharp opacity drops. This is shown in Figure 14 for a gas density $\rho = 10^{-8}$ g cm $^{-3}$, which is typical for the outer regions of protoplanetary disks. Semenov et al. (2003) calculate Rosseland mean opacities in protoplanetary disks for grains of different sizes and structure. As shown in Figure 14, their results are in good agreement with Bell & Lin (1994). However, Semenov et al. (2003) do not take grain growth into account, which is likely to occur in protoplanetary disks, particularly when most solids have been accreted. D'Alessio et al. (2001) compute wavelength dependent opacities for a range of maximum particle sizes and

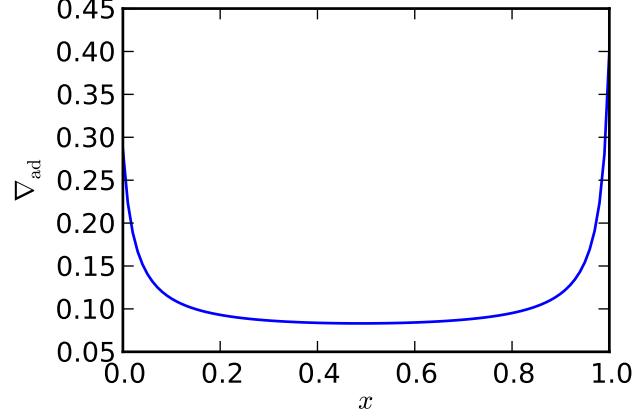


FIG. 13.— Adiabatic gradient as a function of the hydrogen dissociation fraction x . The adiabatic gradient is $\nabla_{\text{ad}} = 2/7$ for pure molecular hydrogen ($x = 0$) and $\nabla_{\text{ad}} = 2/5$ for fully atomic hydrogen ($x = 1$), and drops to low values during partial dissociation.

different size distributions. Figure 14 shows the integrated Rosseland mean opacity for a maximum particle size of 1 cm and a power law size distribution $n \sim a^{-p}$, with a the grain size and $p = 3.5$ for a normal collisional cascade and $p = 2.5$ when coagulation is taken into account. We see in Figure 14 that this yields a mean opacity that is both lower and less sensitive to temperature, when compared to Bell & Lin (1994) or Semenov et al. (2003). However, observations of dust in protoplanetary disks have only been made at low temperatures (i.e., before dust sublimates). As we see in Figure 14, the opacity dramatically decreases during dust sublimation for ISM grains, which can result in regions in the inner parts of planetary atmospheres where energy is transported radiatively, i.e. radiative windows. We thus use the Bell & Lin (1994) opacities for $T \gtrsim 1000$ K, ensuring they smoothly match the D'Alessio et al. (2001) opacities for lower temperatures.

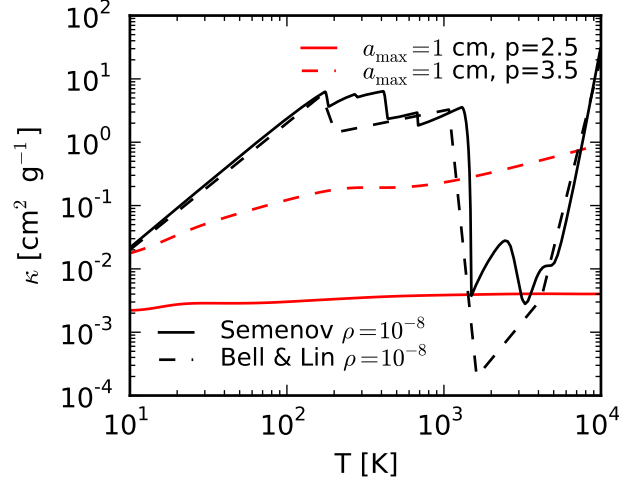


FIG. 14.— Rosseland mean opacity of dust grains as a function of temperature for different opacity assumptions. The dashed black curve shows the Bell & Lin (1994) analytic ISM opacity for $\rho = 10^{-8} \text{ g cm}^{-3}$. The solid black curve shows the tabulated opacity of Semenov et al. (2003) for a dust composition of 'normal' silicates. The dashed red curve shows the D'Alessio et al. (2001) opacity, which takes grain growth into account, for a maximum particle size of 1 cm and a normal collisional cascade grain size distribution ($p = 3.5$). The solid red curve is the same as the dashed red curve, but it accounts for coagulation ($p = 2.5$).

The significant opacity drop due to the sublimation of ice and metal grains lowers the radiative temperature gradient ∇_{rad} , which may result in one or more inner radiative layers inside the atmosphere of a protoplanet. This is displayed in Figure 15: depending on the semi-major axis and core mass, the opacity drop will generate no radiative window (top panel), one radiative window (middle panel), or two radiative windows (bottom panel).

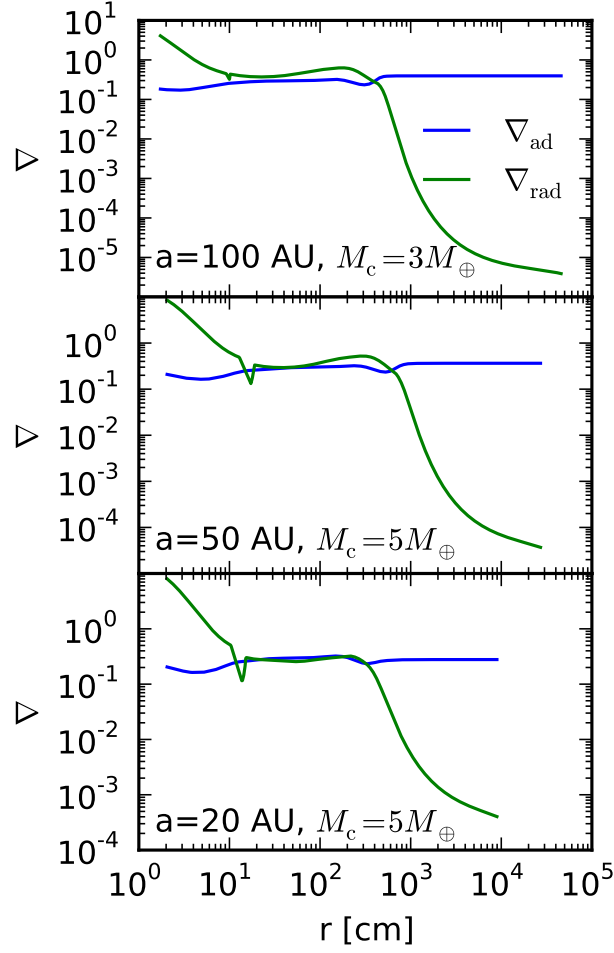


FIG. 15.— Snapshots of the radiative and adiabatic gradient as a function of the radial coordinate, for planets with different core masses forming at various locations in the disk. The sharp drop in opacity due to dust sublimation may generate one or more radiative windows. Top panel: no radiative window for $a = 100$ AU and $M_c = 3M_\oplus$. Middle panel: the opacity drop produces one radiative window for $a = 50$ AU and $M_c = 5M_\oplus$. Bottom panel: the sharp drop in opacity results in two radiative windows for $a = 20$ AU and $M_c = 3M_\oplus$.